Hindawi
Journal of Chemistry
Volume 2022, Article ID 2982594, 12 pages
https://doi.org/10.1155/2022/2982594

Research Article

Enhanced Performance of Sn@Pt Core-Shell Nanocatalysts Supported on Two Different Carbon Structures for the Hydrogen Oxidation Reaction in Acid Media

F. J. Rodríguez-Varela,[1] **G. Hernández-Vázquez**,[1] **S. Dessources**,[2] **B. Escobar-Morales**,[3] **Aruna K. Kunhiraman**,[4] **M. A. Garcia-Lobato**,[5] **and I. L. Alonso-Lemus**[6]

[1]*Sustentabilidad de Los Recursos Naturales y Energía, Cinvestav Unidad Saltillo, Av. Industria Metalúrgica 1062, Parque Industrial Saltillo-Ramos Arizpe, C. P., 25900 Ramos Arizpe, Coah, Mexico*
[2]*Laboratoire des Sciences pour l'Environnement et l'Énergie (LS2E), École Normale Supérieure, Port-au-Prince, Haiti*
[3]*CONACyT, Centro de Investigación Científica de Yucatán, Km. 5.5 Carr. Sierra Papacal-Chuburná Puerto, Tablaje 31257, Sierra Papacal, Yucatán 97302, Mexico*
[4]*Rathinam Research Center, Rathinam Technical Campus, Coimbatore 641021, Tamilnadu, India*
[5]*Facultad de Ciencias Químicas, Universidad Autónoma de Coahuila, C. P., 25280 Saltillo, Coahuila, Mexico*
[6]*CONACyT, Sustentabilidad de los Recursos Naturales y Energía, Cinvestav Unidad Saltillo, Ramos Arizpe, Mexico*

Correspondence should be addressed to F. J. Rodríguez-Varela; javier.varela@cinvestav.edu.mx

Received 3 May 2022; Revised 8 August 2022; Accepted 25 August 2022; Published 12 September 2022

Academic Editor: Hassan Arida

Sn@Pt core-shell nanocatalysts, supported on Vulcan XC-72 and home-developed nitrogen-doped graphene (Sn@Pt/C and Sn@Pt/NG, respectively), were evaluated for the hydrogen oxidation reaction (HOR) in acid electrolyte. The nanocatalysts were synthesized by the bromide anion exchange (BAE) method. TEM characterization confirmed the nanosize nature of Sn@Pt/C and Sn@Pt/NG, with an average particle size of 2.1 and 2.3 nm, respectively. Sn@Pt/C delivered a similar mass limiting current density ($j_{l,\ m}$) of the HOR compared to Sn@Pt/NG, which was higher than those of Pt/C and Pt/NG (ca. 2 and 2.3-fold increase, respectively). Moreover, the Sn@Pt/C and Sn@Pt/NG core-shell nanocatalysts demonstrated a higher specific activity related to Pt/C and Pt/NG. Mass and specific Tafel slopes further demonstrated the improved catalytic activity of Sn@Pt/C for the HOR, followed by Sn@Pt/NG. The application of the nanocatalysts was proposed for polymer electrolyte membrane fuel cells (PEMFC).

1. Introduction

PEMFC have reached important niche energy markets over the past years, such as the automotive industry, stationary power applications, and the so-called poly-generation systems [1, 2]. PEMFC have relevant advantages over conventional systems based on fossil fuels, including the fact that the use of hydrogen (H_2) as the fuel leads to green electrochemical conversion devices [3], in addition to higher energy conversion efficiencies, and zero or very low greenhouse gases (GHG) emissions [1]. Moreover, the concept of green H_2 has gained a great deal of attention recently [4, 5]. On this matter, the feasibility of taking advantage of green H_2 produced by low-temperature electrolyzers using it in PEMFC is highly relevant, because of the prospective of reaching a carbon-neutral international energy scenario.

Despite these advantages, it is acknowledged that the cost of PEMFC systems must be reduced, aiming to be more successful in reaching broader markets [2, 6]. Some breakdown studies indicate that catalysts may account for 41% of the total cost of a fuel cell stack on the basis of 500,000 units produced per year [7]. Thus, strategies to reduce the amount of Pt-group metal (PGM) catalysts in PEMFC have been implemented.

Among those approaches, the development of alloyed, metal-metal oxide, and core-shell Pt-based nanocatalysts

have demonstrated their effectiveness in reducing the amount of this noble metal, maintaining a high catalytic activity for the hydrogen oxidation reaction (HOR) and oxygen reduction reactions (ORR) at the anode and cathode of PEMFC, respectively. Core-shell nanostructures have unique properties, which are of interest for high-performance PEMFC: (i) the modification of the electronic structure of Pt by the core material, which in turn increases the catalytic activity of the nanostructures by changing the adsorption energy of species; (ii) improved electrochemical stability; and (iii) high Pt utilization because of its exposure to active species being the outermost layer [8, 9].

Pt-based core-shell nanocatalysts have probed a high catalytic activity for the ORR in acid media, employing plurimetallic, monometallic, or metal oxides cores such as Pd_3Cu_1, Ni, Ir, Co_3O_4, and $Pd_1Ir_1Ni_2$, among others [8–12]. To the best of our knowledge, the assessment of catalytic activity of Pt-based core-shell nanocatalysts for the HOR in acid media is scarce. Wang et al., report the high performance of Ru@Pt core-shell nanocatalysts with ultra-low Pt content for the HOR in acid media, having a 1 : 1 Ru : Pt atomic ratio [13]. Adzic et al. demonstrate a 2-fold enhancement in catalytic activity for the HOR of Ru@Pt core-shell nanoparticles, compared to Pt-Ru alloys. In that study, the Ru@Pt core-shell having a Pt shell thickness of two monolayers shows an increase in specific activity of the HOR by a factor of 1, compared to monometallic Pt [14].

Elsewhere, several Pt-based core-shell nanostructures having Ru, Rh, or Au as the core have shown a high performance for the HOR, however in alkaline media [15–18]. Nevertheless, the advantages of using supported metal@Pt core-shell nanostructures with a lower Pt content compared to monometallic Pt/C, yet sustaining high performance, encourages the research on those nanocatalysts for the HOR in acid media. On this matter, Sn is an element widely used as cocatalyst of Pt for fuel cell reactions. Because of its higher oxophilicity compared to Pt (0.4 vs. 0.1, respectively) [19], it forms adsorbed OH-species at more negative potentials, transferring them to Pt-sites, facilitating the electrochemical reaction taking place at the noble metal (bifunctional mechanism) [20].

Sn is also significantly cheaper than Pt [21], which results in lower cost Sn@Pt nanocatalysts, also compared to Pt/C. One of the most widely studied applications of Sn as cocatalysts is that for the ethanol oxidation reaction (EOR) at Pt-Sn/C alloys, improving the performance of monometallic Pt/C nanocatalysts through the already mentioned bifunctional mechanism and the electronic effect [22, 23]. Sn has been successfully used in the synthesis of intermetallic, random-alloy, and core-shell Pt-based nanocatalysts [24, 25].

Precisely, one of the most effective methods of synthesis of noble metal nanocatalysts is the bromide anion exchange (BAE) process. Early reports highlight the advantages of implementing this surfactant-free method, which include the following: (i) avoiding the presence of organic molecules that may prevent the adsorption of active species at the metal sites of the nanocatalysts; (ii) controlling the particle size growth, enhancing the electrochemically active surface area (ECSA); and (iii) being a suitable and straightforward, environmentally friendly method [26–28].

In this work, Sn@Pt/C and Sn@Pt/NG nanocatalysts (where *C*: commercial Vulcan XC-72 and NG: home-synthesized *N*-doped graphene) have been synthesized by the BAE method. Their catalytic activity for the HOR is characterized by acid electrolyte and compared to that of monometallic Pt/C and Pt/NG.

2. Experimental

2.1. Heat Treatment of Vulcan XC-72 and Synthesis of Nitrogen-Doped Graphene (NG). Vulcan powders were heat treated at 400°C for 4 h in N_2 atmosphere, aiming to eliminate surface impurities [29]. NG was obtained by mixing graphite flakes and urea in a 10 : 90 wt. ratio. The mixture was submitted to ball milling using a Restch PM 200 apparatus in a balls: material weight ratio of 5 : 1, at 300 rpm for 8 h, pausing for 30 min after every hour of milling. The resulting material was passivated in N_2 for 12 h, followed by pyrolysis at 500°C in N_2 atmosphere for 1 h.

2.2. Synthesis of Core-Shell Nanocatalysts by the Bromide Anion Exchange (BAE) Method. KBr and $NaBH_4$ were used as solvents and reducing agents, respectively, [30]. Nominally, a metal: carbon weight ratio of 20 : 80 was expected for the core-shell nanostructures, with a theoretical Pt : Sn atomic ratio of 1 : 1. As an example, for the synthesis of Sn@Pt/C, in the first step Sn/C was synthesized as follows: 21.57 mg of $SnCl_6{\cdot}2H_2O$ were stirred in 95.6 mL deionized water for 5 min, followed by the addition of 16.6 mg of KBr maintaining agitation for 10 min ($n_{KBr}/n_{metallic\ salt}$ ratio = 1.46). A solution containing 120 mg of *C* was adjusted to the mixture, which was submitted to ultrasound for 45 min. Afterward, 14.3 mL of a 0.1 M $NaBH_4$ solution was added ($n_{NaBH4}/n_{metallic\ salt}$ ratio = 15), applying magnetic stirring at 40°C for 2 h. The obtained powders were filtered, washed with deionized water, and dried at 50°C for 12 h.

In a second step, the Pt shell was deposited on the core material by stirring 48.2 mg of $H_2PtCl_6{\cdot}6H_2O$ in 92.9 mL of deionized water for 5 min, with the subsequent addition of 16.15 mg of KBr keeping agitation for 20 min ($n_{KBr}/n_{metallic\ salt}$ ratio = 1.46). To this mixture, 128 mg of Sn/C were adjusted, followed by ultrasound agitation for 45 min. Then, 13.9 mL of 0.1 M $NaBH_4$ were added by applying magnetic stirring at 40°C for 2 h ($n_{NaBH4}/n_{metallic\ salt}$ ratio = 15). The powders were filtrated, washed with deionized water, and dried at 50°C for 12 h. Sn@Pt/NG, Pt/C, and Pt/NG were obtained following the same procedure.

2.3. Physicochemical and Electrochemical Characterization. Details of the physiochemical and electrochemical characterization were reported previously [31–34]. Briefly, textural properties of the supports were obtained in a Quantachrome Instruments Autosorb1 analyzer. XRD patterns were acquired in a Bruker D2 Phaser apparatus in the 2θ interval from 10 to 100°. Crystallite size was determined using the following Scherrer equation:

$$d = \frac{k \cdot \lambda}{B \cdot \cos(\theta)}, \quad (1)$$

where $k = 0.9$, λ is the wavelength of the X-rays (0.1541 nm), B is the full width at half height of the reflection, and θ is the peak maximum of the reflection. The lattice parameter a_{fcc} was calculated from the following equation:

$$a_{fcc} = \frac{\sqrt{2} \cdot \lambda}{\sin(\theta)}. \quad (2)$$

The chemical composition reported is the average of 5 micro areas analyzed by EDS in a Philips XL30 SEM microscope. Characterization by TEM was performed in a Jeol 2100 microscope, operating at 200 kV. XPS analysis was carried out using a Thermo Scientific *K*-Alpha + XPS apparatus (hv = 1486.68 eV).

A three-electrodes setup was used for electrochemical characterization in 0.5 M H_2SO_4, using a WaveDriver 20 bipotentiostat equipped with a rotating disc electrode setup (Pine Inst.). The reference electrode was an Ag/AgCl (saturated KCl), while the counter was a Pt coil, both placed in separated chambers from the main electrolyte. The working electrode was a 5 mm diam glassy carbon. Catalyst inks were prepared by dispersing for 30 min in ultrasound 5 μL Nafion® solution, 1 mL 2-propanol, and 10 mg of nanocatalyst powder. Aliquots of 10 μL were deposited on the glassy carbon. All potentials were reported on the RHE scale.

Cyclic voltammograms (CV) were acquired in the 0.05–1.2 V vs. RHE interval at 20 $mV \cdot s^{-1}$ in N_2 atmosphere. The electrochemically active surface area ($ECSA_H$) and the real area (A_r) were determined to take the charge due to the desorption of hydrogen in the hydrogen adsorption/desorption region ($H_{ads/des}$) of the CV, according to the following equations:

$$ECSA_H = \frac{Q}{Q_{H \cdot L_{Pt}}}, \qquad A_r = \frac{Q}{Q_H}. \quad (3)$$

where Q is the experimental electrical charge due to the desorption of hydrogen; Q_H is the theoretical charge due to the desorption of one monolayer of hydrogen on Pt (210 $\mu C \cdot cm^{-2}$); and L_{Pt} is the Pt loading on the electrode.

Accelerated degradation tests (ADT) were performed on the nanocatalysts by submitting them to 1000 cycles in the same potential interval indicated above, at a scan rate of 200 $mV \cdot s^{-1}$. CO-stripping polarization curves were obtained by bubbling CO for 10 min, while polarizing the working electrode at 0.05 V vs. RHE, then purging it by flowing N_2 in the electrolyte for 20 min. CV was acquired in the same mentioned potential window at 20 $mV \cdot s^{-1}$.

The catalytic activity of the nanocatalysts for the HOR was evaluated in a rotating disc setup. H_2 was bubbled in the acid electrolyte for 20 min, after which polarization curves were plotted at rotation rates ω of 400, 800, 1200, 1600, and 2000 rpm, in the 0–0.65 V vs. RHE range. Curves compensated for iR drop were reported in this work. The R value of the 0.5 M H_2SO_4 was determined from EIS measurements. Koutecky–Levich plots were obtained using the well-known Levich equation as follows:

$$\frac{1}{j} = \frac{1}{j_k} + \frac{1}{j_d}, \quad (4)$$

where j_d, j_k, and j are the diffusion-controlled, kinetic, and measured current density, respectively. The kinetic current i_k was obtained with the following equation:

$$i_k = \frac{i_d \cdot i}{i_d - i}, \quad (5)$$

where i_d and i are the diffusion-controlled and measured current, respectively. From equation (5), mass and specific Tafel plots were obtained by normalizing i_k by the Pt mass content and A_r, respectively.

3. Results and Discussion

Figure 1 shows the XRD patterns of the nanocatalysts. Pt/C has reflections ascribed to (002) due to the graphitic zones in the structure of Vulcan, and the (111), (200), (220), (311), and (222) planes of the fcc structure of Pt (PDF 00-004-0802). Sn@Pt/C shows the same peaks, with similar features. Moreover, no noticeable shift in the position of the peaks between the monometallic and the core-shell nanocatalysts has been observed. Such characteristic suggests that no atoms of the Sn core have incorporated into the Pt shell contracting it and provoking the formation of alloyed phases, as has been reported elsewhere for some other core-shell nanostructures [35, 36]. Additionally, the broadness of the reflections suggests the nanosized feature of the anode materials.

Meanwhile, Pt/NG and Sn@Pt/NG have an intense reflection due to the (002) plane characteristic of graphene-like structures, as well as the (101) and (004) peaks also ascribed to the support [37]. Moreover, both nanocatalysts show the peaks attributed to fcc Pt, also without a noticeable shift in their position.

Figure S1 in the supplementary information file shows the XRD patterns of the graphite flakes, NG, and Vulcan. The first two have high-intensity and low-intensity very narrow peaks at $2\theta = 26.5$ and 54.54°, attributed to the (002) and (004) carbon planes, characteristic of graphitic materials, respectively. These characteristics support the observations in the previous paragraph of the patterns shown in Figure 1. Vulcan shows broader peaks due to the (002) and (101) reflections of carbon at $2\theta = 25$ and 44.39°, respectively. The position of the (002) plane in Vulcan correlates well with previous reports in the literature [38]. Overall, graphite and NG show crystalline features, while Vulcan is rather amorphous in nature.

Features of the nanocatalysts from Figure 1 are shown in Table 1. The crystallite size (d_{XRD}) ranges from 3.4 to 6.1 nm, the smallest one being that of Sn@Pt/C, while the nanocatalysts supported on NG have larger values. Interestingly, there is no variation in lattice parameter (a_{fcc}) when comparing the monometallic nanocatalysts to the core-shell Sn@

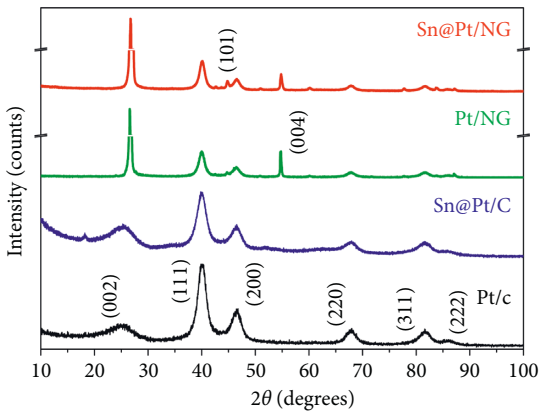

Figure 1: XRD patterns of Pt/C, Sn@Pt/C, Pt/NG, and Sn@Pt/NG.

Table 1: Parameters of the nanocatalysts from XRD and TEM analysis.

Nanocatalyst	d_{XRD} (nm)	a_{fcc} (nm)	d_{TEM} (nm)
Pt/C	4.0	0.3906	—
Pt/NG	6.1	0.3917	—
Sn@Pt/C	3.4	0.3906	2.1
Sn@Pt/NG	6.0	0.3917	2.3

Pt nanostructures on each carbon support, which indicates that the Pt lattice has suffered no contraction.

Figure S2 shows the Raman spectra of graphite, NG, and Vulcan. Peaks ascribed to the *D*, *G*, and 2*D* bands are observed at 1350, 1580, and 2670 cm^{-1}, respectively. The *G* band originates because of the stretching of sp^2 C-C bonds, and it is related to the structural order of the carbon material [39]. The *D* and 2*D* bands emerge from stretching vibrations of hybridized sp^2 and sp^3 bonds, indicating the degree of structural disorder of the samples [39]. Thus, the ratio of the relative intensities of the *D* and *G* bands (I_D/I_G) is an indicator of the degree of structural disorder or crystallinity of the materials [40].

Graphite has an I_D/I_G ratio of 0.04, confirming its highly crystalline structure. NG has the same peaks as graphite. However, the relative intensity of its *D* band increases considerably, resulting in $I_D/I_G = 0.86$. Such a result confirms the structural modification of NG, i.e., an increased disorder suggesting the formation of graphene layers or exfoliated graphite after ball milling. Moreover, the increased disorder observed for NG can be attributed to the doping with heteroatoms [39]. Meanwhile, Vulcan has an I_D/I_G ratio of 1.49, evidencing its disordered characteristic.

Table 2 shows the chemical composition of the nanocatalysts from EDS analysis. The Pt content at Pt/C and Pt/NG is lower than nominally expected, although the O concentration is higher than 2 wt. %. Moreover, 3.27 wt. % of *N* has been detected at Pt/NG, which has a C content close to 80 wt. % theoretically expected. On the other hand, the C content at Sn@Pt/C is higher than the nominal one, while Sn@Pt/NG shows 81.81 of this element, along with 5.68 (wt. %) of N. Meanwhile, the Pt : Sn ratio at Sn@Pt/C and Sn@Pt/NG is higher than theoretically expected.

Table 2: Chemical composition of the nanocatalysts by EDS.

Electrocatalizador	Pt	Sn	C	O	N	Pt : Sn at. ratio
	(wt. %)					
Pt/C	14.18	—	83.50	2.32	—	—
Pt/NG	14.89	—	79.16	2.68	3.27	—
Sn@Pt/C	8.29	1.60	86.22	3.89	—	3.1 : 1
Sn@Pt/NG	6.25	1.43	81.81	4.83	5.68	2.7 : 1

— Not determined.

Figure 2(a) (top) shows (A) the TEM micrograph of Sn@Pt/C, where the histogram (inset) indicates an average particle size $d_{TEM} = 2.1$ nm (Table 1). Figure (B) is an HRTEM micrograph of the core-shell nanocatalyst. FFT analysis allows to characterization of the nanoparticles by generating SAED patterns (inset). Two interplanar distances have been determined: (i) 0.195 nm at the center of the nanoparticle, which has been ascribed to the (211) reflection of Sn [41], even though the (200) peak of Pt may have a somehow similar value [42]; (ii) 0.220 nm at the border of the nanoparticle, attributed to the (111) plane of Pt [43]. Figure (C) shows the micrograph in dark field mode.

Figure 2(b) (bottom) shows the same analysis for Sn@Pt/NG. Inset in (A) reveals a d_{TEM} value of 2.3 nm (Table 1). Analysis by FFT in (B) also demonstrates two interplanar distances at this nanocatalyst: (i) 0.198 nm at the center ascribed to Sn (211); (ii) 0.216 nm at the border ascribed to Pt (111). Figure (C) is the dark field micrograph of the nanocatalyst. These features support the core-shell nature of nanostructured Sn@Pt/C and Sn@Pt/NG.

Table S1 depicts the surface chemical composition of the nanocatalysts by XPS. Under this perspective, the nanocatalysts have a Pt concentration between 0.68 and 2.97 (at. %). Interestingly, the Pt : Sn at. ratio of Sn@Pt/C and Sn@Pt/NG reaches a value closer to the nominal than in Table 2, more clearly seen at Sn@Pt/C (1.0 : 0.87). It is noteworthy that by using the XPS technique, no *N* species have been detected at the nanocatalysts supported on NG. Such difference compared to EDS analysis (Table 2) has been attributed to the sensitivity of XPS, which is a superficial characterization technique.

The high-resolution XPS spectra of Pt/C in the Pt 4f region is shown in Figure 3(a). Two doublets due to the spin-orbit splitting into the Pt4$f_{7/2}$ and Pt4$f_{5/2}$ states are observed. Pt^0 and Pt^{2+} species are identified at the nanocatalyst [43], the former having a higher relative concentration (Table S2). Similar doublets can be seen at Pt/NG (Figure 3(b)), also having a higher concentration of Pt^0 compared to Pt^{2+} species (Table S2).

Figures 3(c) and 3(d) are the high-resolution spectra in the Pt 4f region of Sn@Pt/C and Sn@Pt/NG, respectively. Both core-shell nanostructures show the two doublets in the Pt4$f_{7/2}$ and Pt4$f_{5/2}$ states. As in the case of the monometallic nanocatalysts mentioned above, both core-shell nanostructures develop a higher relative concentration of Pt^0 compared to Pt^{2+} (Table S2). Figures 3(e) and 3(f) show the spectra of Sn@Pt/C and Sn@Pt/NG in the Sn 3d region. In both cases, only Sn^{2+} (SnO) has been detected in the splitting into the Sn3$d_{5/2}$ and Sn3$d_{3/2}$ states, i.e., no metallic Sn has

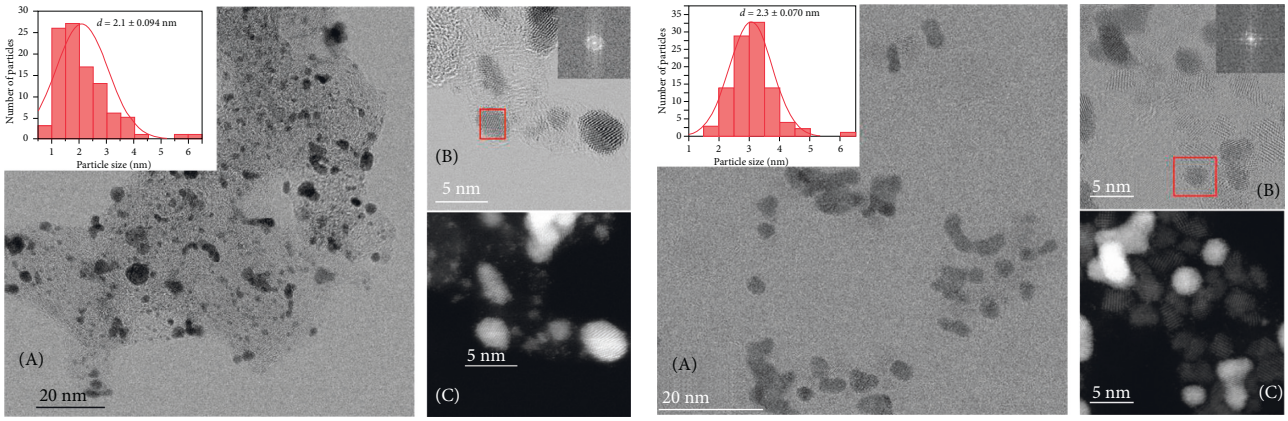

Figure 2: HRTEM micrographs of Sn@Pt/C and Sn@Pt/NG.

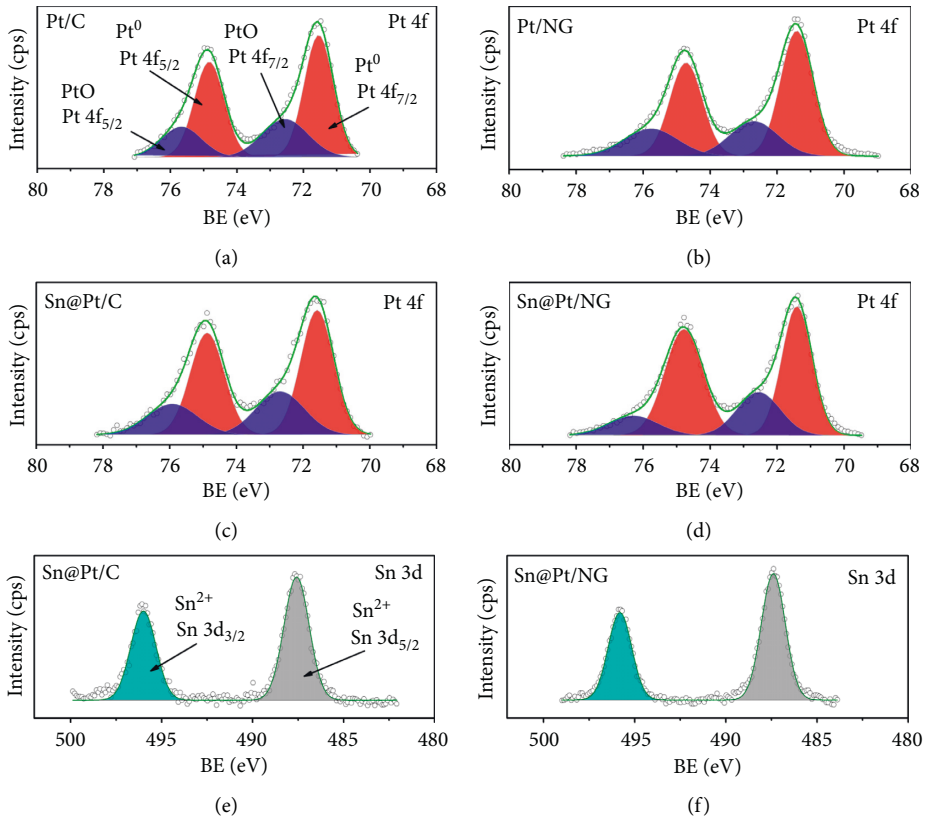

Figure 3: High-resolution XPS spectra in the Pt 4f region of (a) Pt/C, (b) Pt/NG, (c) Sn@Pt/C, and (d) Sn@Pt/NG. (e)-(f) High-resolution spectra in the Sn 3D region of Sn@Pt/C and Sn@Pt/NG.

been formed at the nanocatalysts. These results confirm the observations in Figure 1, where no reflections associated with metallic Sn have emerged.

Figures S3 and S4 show the spectra of the nanocatalysts in the C 1 s and O 1 s regions, respectively. In particular, the presence of PtO bonds at the nanocatalysts in Figure S4 correlates well with the development of Pt^{2+} species in the Pt 4f region in Figure 3. The other bonds are typically observed at carbon-supported Pt nanocatalysts [33].

Figure 4 shows CVs of (a) Pt/C, (b) Pt/NG, (c) Sn@Pt/C, and (d) Sn@Pt/NG before (1^{st} cycle) and after (1000^{th} cycle) ADT. Considering the chemical composition reported in Table 2, the total metal loading at the working electrodes is 72.3, 75.9, 51.2, and 39.18 mg cm^{-2} at Pt/C, Pt/NG, Sn@Pt/C,

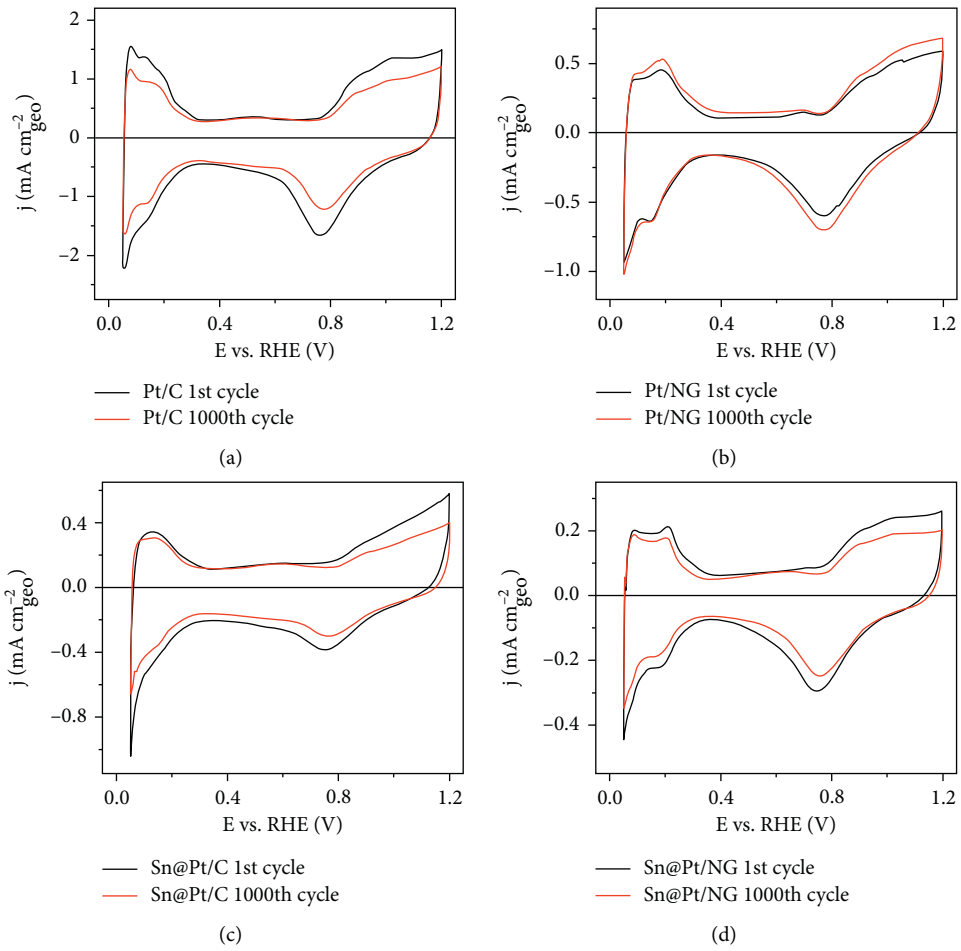

Figure 4: CVs of the nanocatalysts before and after ADT. (a) Pt/C, (b) Pt/NG, (c) Sn@Pt/C, (d) Sn@Pt/NG. Electrolyte: 0.5 M·H_2SO_4 saturated with N_2. Scan rate: 20 mV·s^{-1}.

Table 3: Electrochemical parameters of the nanocatalysts from CV and CO-stripping tests.

Nanocatalyst	A_r (cm$_r^{-2}$)	ECSA$_H$ ($m^2 \cdot g_{Pt}^{-1}$)	ECSA$_H$* ($m^2 \cdot g_{Pt}^{-1}$)	Variation (%)	ECSA$_{CO}$ ($m^2 \cdot g_{Pt}^{-1}$)	j_{CO} (V/RHE)	$E_{onset,\ CO}$ (V/RHE)
Pt/C	8.05	57.10	38.43	-32.7	85.17	0.76	0.54
Pt/NG	2.82	19.06	19.82	3.9	26.07	0.67,0.72	0.35
Sn@Pt/C	1.33	16.32	15.80	-3.2	21.89	0.67,0.72	0.40
Sn@Pt/NG	1.25	20.18	17.18	-14.87	22.50	0.67,0.77	0.40

*Value after ADT.

and Sn@Pt/NG, respectively. A typical negative variation in j is observed after ADT at three of the nanocatalysts ascribed to agglomeration and segregation of nanoparticles, while Pt/NG has an increase after cycling over the potential window, which suggests the activation of Pt sites due to the test.

As indicated, the electric charge due to desorption within the $H_{ads/des}$ region has been used to determine their A_r before ADT, and their ECSA$_H$ at the 1st and 1000th cycle. Table 3 shows the values of these parameters. Pt/C has the largest A_r and ECSA$_H$ values before ADT. In fact, its ECSA$_H$ is similar to previous reports elsewhere on analogous Pt/C nanocatalysts [23]. Nevertheless, Pt/C has the most important negative variation in ECSA$_H$ (-32.7%), of the same order as reported previously [23], and roughly 10 times higher than that of the Sn@Pt/C core-shell nanocatalyst. Pt/NG shows high stability and even gains active surface area after ADT. Meanwhile, Sn@Pt/NG shows a more important negative variation in ECSA$_H$ than Sn@Pt/C.

The active surface area has also been determined from CO-stripping tests (ECSA$_{CO}$) before ADT, as shown in Figure S5, where the first cycle is the CO oxidation, while the second one indicates the behavior of the clean surface of the nanocatalysts in the N_2-saturated electrolyte. Table 3 shows the ECSA$_{CO}$ values obtained, which overall are higher than their ECSA$_H$ counterparts. The nanocatalyst with the highest ECSA$_{CO}$ value is also Pt/C, while the tendency at the other nanocatalysts resembles that of ECSA$_H$ before ADT.

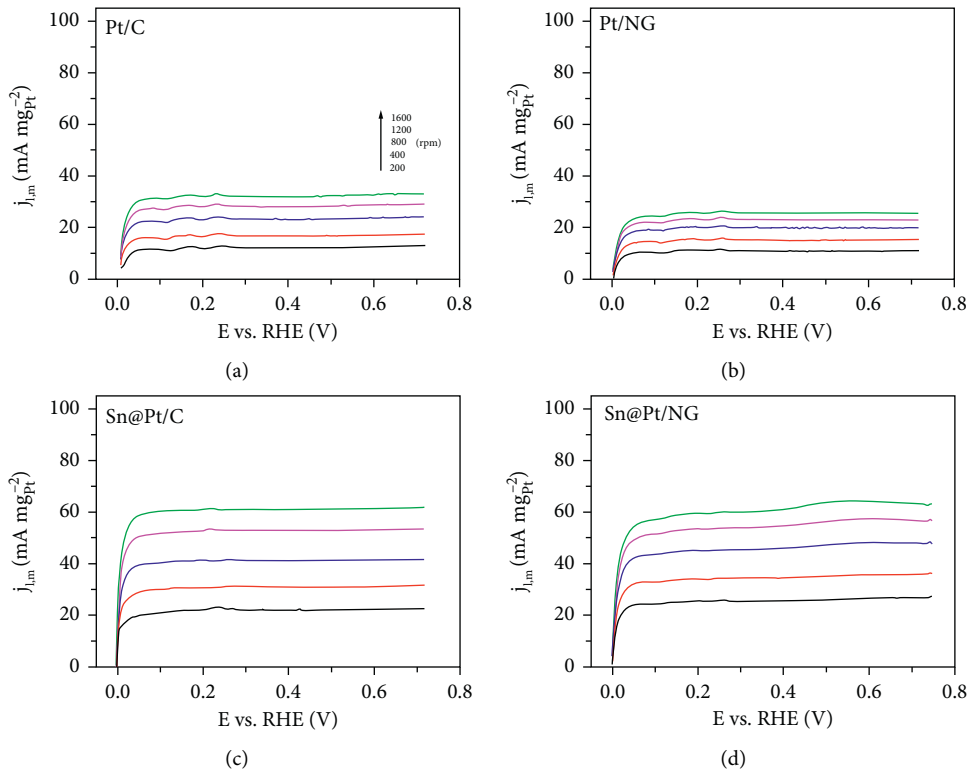

Figure 5: Mass activity of the HOR at (a) Pt/C, (b) Pt/NG, (c) Sn@Pt/C, and (d) Sn@Pt/NG at several ω. Electrolyte: H_2-saturated 0.5 M·H_2SO_4. Scan rate: 5 mV·s^{-1}.

Moreover, the shape of the CO oxidation plots shows the effect of both the chemical composition of the nanocatalysts and the type of support used. Pt/C has a characteristic narrow peak of monometallic Pt nanocatalysts supported on Vulcan [44], with a maximum current density peak due to the oxidation of CO (j_{CO}) at 0.76 V/RHE and an onset potential ($E_{onset,\ CO}$) of 0.54 V/RHE (Table 3). The use of the NG support has an important effect on Pt/NG by shifting $E_{onset,\ CO}$ by 0.19 V toward more negative values compared to Pt/C. Additionally, a broad shoulder with two peaks (0.67 and 0.72 V/RHE) is observed at Pt/NG, different than the sharp peak at Pt/C. This behavior of monometallic Pt has been ascribed to arbitrary nucleation of Pt nanoparticles onto sp^2 and sp^3 carbon domains [44].

Interestingly, despite being supported on Vulcan, Sn@Pt/C also shows a broad shoulder with two peaks, i.e., there is a significant effect of the chemical composition of the nanocatalyst on the oxidation of CO. Such behavior has been attributed elsewhere to two Pt states induced at a Pt shell by a Ru core [45], which is analogous to the effect of Sn on the Pt shell in this work. Moreover, the fact that the two peaks shown by Sn@Pt/C are at more negative potentials (0.67 and 0.72 V/RHE, Table 3) than that of Pt/C, indicates a displacement of the *d*-band center of the Pt shell due to a compressive strain effect provoked by the Sn core [45]. Additionally, $E_{onset,\ CO}$ = 0.4 V/RHE at Sn@Pt/C, i.e., more negative than Pt/C, although 50 mV more positive than Pt/NG.

Meanwhile, Sn@Pt/NG shows peaks at 0.67 and 0.77 V/RHE, ascribed to an effect of both carbon support and chemical composition of the nanocatalyst, with $E_{onset,\ CO}$ = 0.4 V/RHE (Table 3). Elsewhere, CO-stripping has been proposed as an electrochemical tool to characterize core-shell nanostructures [46]. The shape of the CO-stripping curves of Sn@Pt/C and Sn@Pt/NG in Figure S5 differs completely from those of Pt-Sn/C alloyed nanocatalysts in [23], which provides more evidence that effectively core-shell nanostructures have been obtained following the synthesis procedure proposed in this work.

Table 4: Mass, specific, and geometric limiting currents of the HOR at 0.4 V/RHE and 1600 rpm on the nanocatalysts.

Nanocatalyst	$j_{l,\ m}$ (mA·mg_{Pt}^{-1})	$j_{l,\ s}$ (mA·cm_r^{-2})	$j_{l,\ geo}$ (mA·cm^{-2})
Pt/C	31.88	0.055	2.29
Pt/NG	25.64	0.134	1.93
Sn@Pt/C	61.08	0.376	2.55
Sn@Pt/NG	61.20	0.303	1.93

The iR-compensated mass polarization curves of the HOR at (a) Pt/C, (b) Pt/NG, (c) Sn@Pt/C, and (d) Sn@Pt/NG are shown in Figure 5. It should be mentioned that an *R* value of about 6 W has been determined for the electrolyte, in good agreement with the literature [47, 48]. A compensation of 80% of the electrolyte resistance has been considered in the plots [49]. As can be observed, at 0.4 V/RHE and 1600 rpm, the mass limiting current density ($j_{l,\ m}$) is significantly higher at Sn@Pt/C and Sn@Pt/NG with an almost 2-fold increase compared to Pt/C and even larger related to Pt/NG (Table 4), demonstrating an important

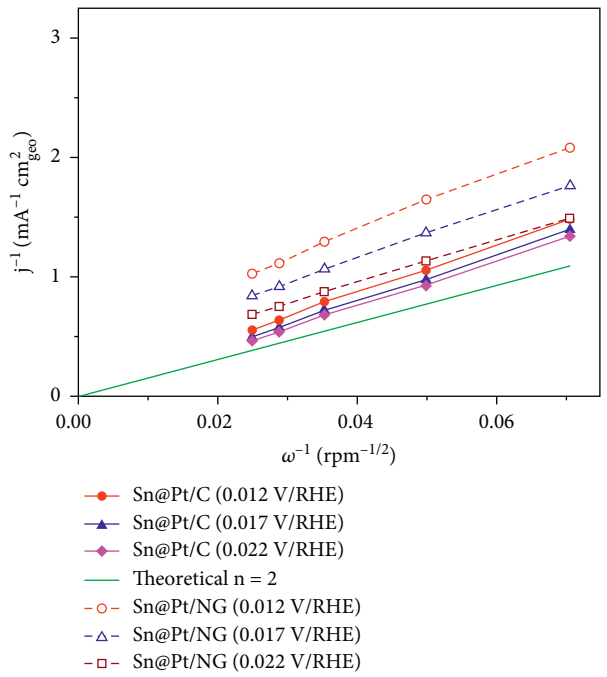

Figure 6: Koutecky–Levich plots of the HOR at Sn@Pt/C and Sn@Pt/NG at several ω. Potentials: 0.012, 0.017, and 0.22 V/RHE. The theoretical slope of $n = 2$ is also shown.

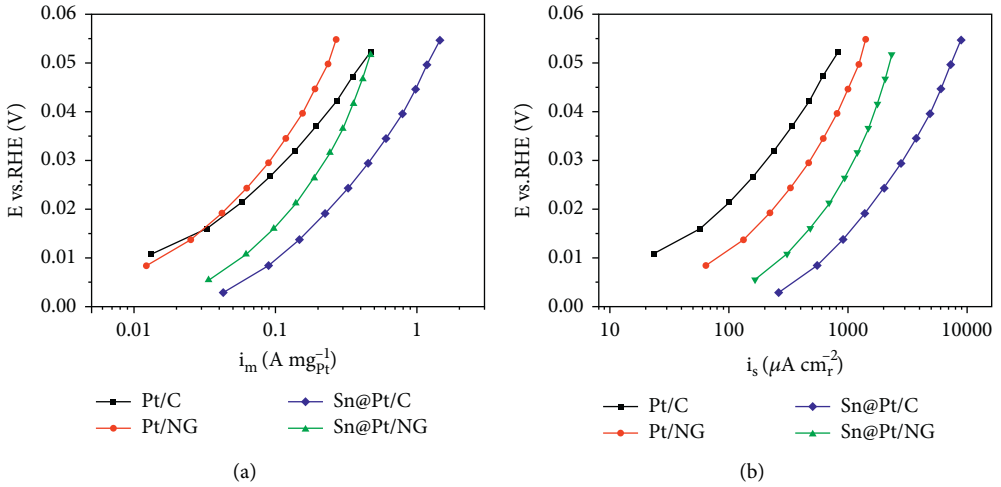

Figure 7: Tafel plots of (a) mass and (b) specific activity of the nanocatalysts for the HOR.

positive effect of applying the core-shell nanostructures to promote the HOR. The $j_{l,\,m}$ value is about the same for the two core-shell nanostructures, suggesting a dominant promotion of the reaction by the Sn@Pt nanoparticles, rather that the use of the NG support.

Furthermore, the specific activity of the nanocatalysts for the HOR is shown in Figure S6. The specific limiting current density ($j_{l,\,s}$) is clearly higher at Sn@Pt/C and Sn@Pt/NG, compared to Pt/C (which has the lowest performance) and Pt/NG (Table 4). In fact, Sn@Pt/C shows an almost 7 and 3-fold increase in $j_{l,\,s}$ related to Pt/C and Pt/NG, respectively. Moreover, Sn@Pt/C demonstrates a higher geometric catalytic activity than the other nanocatalysts, as seen in Figure S7 and Table 4. Thus, based on the mass, specific, and geometric data in Table 4, Sn@Pt/C has the highest catalytic activity for the HOR, followed by Sn@Pt/NG.

Figure 6 shows the Koutecky–Levich plots of the HOR at Sn@Pt/C and Sn@Pt/NG, obtained from Equation (4). A theoretical Koutecky–Levich plot of a mechanism of the HOR involving a $2\,e^-$ transfer has been obtained with the following equation [50, 51]:

$$\frac{1}{B} = \frac{1}{0.2nF\nu^{-1/6}D_{H_2}^{2/3}C_{H_2}}, \tag{6}$$

where the Koutecky–Levich slope is $1/B$, while n: number of electrons transferred ($n = 2$); F: Faraday constant (96, 500°C); ν: kinematic viscosity (0.01 cm^2·s^{-1}); D: hydrogen diffusion

Table 5: Comparison of performance of Sn@Pt/C with those of the literature.

Nanocatalyst	Electrolyte/rotating rate (rpm)	$j_{l,\ geo}$ (mA cm^{-2})	i_m (A mg_{Pt}^{-1})	i_s (mA cm_r^{-2})	Ref.
Sn@Pt/C	0.5 M H_2SO_4/1600	2.55	1.18[a]	7.27	This work
TKK 46% Pt/C	0.1 M $HClO_4$/900	2.25	n.a.	n.a.	[52]
Polycrystalline Pt	0.1 M $HClO_4$/1600	2.90	n.a.	n.a.	[53]
Polycrystalline Pt	$HClO_4$ (pH = 0.2)/1600	2.75	n.a.	n.a.	[54]
RuO_2-Pt/C	$HClO_4$ (pH = 1.09)/1600	2.75	n.a.	n.a.	[55]
PtMo-CeOx-NAs	0.1 M $HClO_4$/1600	2.75	3.49[a]	15	[56]
Pt–PdO/C	0.1 M $HClO_4$/1600	2.50	0.127[b,c]	n.a.	[57]

[a]At 50 mV vs. RHE; [b]at 200 mV vs. RHE; [c]total metal loading; n.a.: not available.

coefficient (3.7×10^{-5} $cm^2 \cdot s^{-1}$); and C_{H2}: concentration of H_2 in H_2SO_4 (7.14×10^{-7} $mol \cdot cm^{-3}$) [38]. As can be seen in Figure 6, the experimental slopes approach the theoretical one, strongly suggesting that the HOR at the core-shell nanocatalysts undergo a mechanism involving a $2\,e^-$ transfer, in good agreement with the HOR reaction in acid media as follows:

$$H_2 \longrightarrow 2H^+ + 2e^-. \quad (7)$$

Tafel plots of mass and specific activity of the nanocatalysts for the HOR are shown in Figures 7(a) and 7(b), respectively. In both scenarios, the catalytic activity decreases in the order Sn@Pt/C > Sn@Pt/NG > monometallics. Thus, there is a significant promotion effect of the core-shell nanostructures for the reaction, which is ascribed to an electronic effect (modification of the Pt *d*-band center due to interactions of the shells with the Sn cores). The bifunctional mechanism, due to the oxophilicity of Sn, may have also contributed to the high performance of the core-shell nanocatalysts.

Table 5 shows a comparison of catalytic activity of Sn@Pt/C with that of some nanocatalysts reported in the literature in acid media. It should be mentioned that most of the data are rough values determined from the plots reported at each work. When considering $j_{L,\ geo}$ (which is the most widely reported), Sn@Pt/C performs very well, with a value of 2.55 $mA \cdot cm^{-2}$, which is slightly higher than that reported for a TKK 46% Pt/C nanocatalyst [52]. In some cases, polycrystalline Pt [53, 54], RuO_2-Pt/C [55], and PtMo-CeOx-NAs [56] show a higher $j_{L,\ geo}$. Meanwhile, the value reported for a Pt-PdO/C nanocatalyst is similar to that of Sn@Pt/C [57].

Attention should be paid, however, to the mass and specific activities for the HOR. The i_m and i_s values of Sn@Pt/C are roughly one-third and one-half of those reported by Cui et al. for their PtMo-CeOx-NAs nanocatalyst, respectively, [56]. Meanwhile, the i_m of Sn@Pt/C is higher than that of the Pt-PdO/C nanocatalyst reported by Barman et al., even though the authors report the mass activity by total metal loading [57]. Thus, further studies should focus on increasing the mass and specific activities of Sn@Pt/C.

4. Conclusions

The BAE method produced nanostructured catalysts. Physicochemical and electrochemical characterizations showed the formation of Sn@Pt/C and Sn@Pt/NG core-shell nanocatalysts. From XPS analysis, Pt^0 and Pt^{2+} species were detected at all nanocatalysts, while only Sn^{2+} formed at Sn@Pt/C and Sn@Pt/NG. CO-stripping tests provided evidence of a displacement of the Pt *d*-band center of the Pt shells because of a strain effect attributed to the Sn cores. Such electronic modification, as well as the bifunctional mechanism due to the oxophilicity of Sn, contributed to the higher mass and specific catalytic activity of the core-shell nanocatalysts for the HOR, particularly Sn@Pt/C. Both Sn@Pt/C and Sn@Pt/NG promoted the HOR via a $2\,e^-$ transfer mechanism.

Data Availability

The data used to support this study are included within the supplementary information files.

Conflicts of Interest

The authors declare that they have no conflicts of interest.

Acknowledgments

This study was supported by the National Council for Science and Technology (Conacyt), Mexico (CB-2015-250632 and CB-2014-241526).

Supplementary Materials

Figures S1 and S2 show the XRD patterns and the Raman spectra of graphite, NG, and Vulcan, respectively. Table S1 depicts the chemical composition of the nanocatalysts as determined by XPS. Table S2 shows the parameters of the nanocatalysts, obtained from XPS analysis. Figures S3 and S4 show the high-resolution spectra in the C 1 s and O 1 s regions of the nanocatalysts, respectively. Figure S5 depicts the CVs resulting from the CO-stripping test at the nanocatalysts. Figure S6 shows the polarization curves of the HER (specific activity) at the nanocatalysts. Figure S7 shows the polarization curves of the HER (geometric activity) at the nanocatalysts. (*Supplementary Materials*)

References

[1] J. Rodríguez-Varela, I. L. Alonso-Lemus, O. Savadogo, and K. Palaniswamy, "Overview: Current trends in green electrochemical energy conversion and storage," *Journal of Materials Research*, vol. 36, pp. 4071–4083, 2021.

[2] A. Baroutaji, A. Arjunan, J. Robinson, T. Wilberforce, M. A. Abdelkareem, and A. G. Olabi, "PEMFC poly-generation systems: developments, merits, and challenges," *Sustainability*, vol. 13, no. 21, Article ID 11696, 2021.

[3] I. Aleknaviciute, T. G. Karayiannis, M. W. Collins, and C. Xanthos, "Towards clean and sustainable distributed energy system: the potential of integrated PEMFC-CHP," *International Journal of Low Carbon Technologies*, vol. 11, no. 3, pp. 296–304, 2016.

[4] G. Squadrito, A. Nicita, and G. Maggio, "A size-dependent financial evaluation of green hydrogen-oxygen co-production," *Renewable Energy*, vol. 163, pp. 2165–2177, 2021.

[5] P. Abmann, A. S. Gago, P. Gazdzicki, K. A. Friedrich, and M. Wark, "Toward developing accelerated stress tests for proton exchange membrane electrolyzers," *Current Opinion in Electrochemistry*, vol. 21, pp. 225–233, 2020.

[6] M. M. Whiston, I. L. Azevedo, S. Litster, K. S. Whitefoot, C. Samaras, and J. F. Whitacre, "Expert assessments of the cost and expected future performance of proton exchange membrane fuel cells for vehicles," *Proceedings of the National Academy of Sciences*, vol. 116, no. 11, pp. 4899–4904, 2019.

[7] S. T. Thompson, B. D. James, J. M. Huya-Kouadio et al., "Direct hydrogen fuel cell electric vehicle cost analysis: System and high-volume manufacturing description, validation, and outlook," *Journal of Power Sources*, vol. 399, pp. 304–313, 2018.

[8] S. J. Hwang, S. J. Yoo, J. Shin et al., "Supported core@shell electrocatalysts for fuel cells: close encounter with reality," *Scientific Reports*, vol. 3, no. 1, p. 1309, 2013.

[9] Z. Yan, Y. Zhang, C. Dai et al., "Porous, thick nitrogen-doped carbon encapsulated large PtNi core-shell nanoparticles for oxygen reduction reaction with extreme stability and activity," *Carbon*, vol. 186, pp. 36–45, 2022.

[10] H.-B. Zheng, L. An, Y. Zheng et al., "Tuning the catalytic activity of Ir@Pt nanoparticles through controlling Ir core Size on cathode performance for PEM fuel cell application," *Frontiers of Chemistry*, vol. 6, p. 299, 2022.

[11] S. Hu, Y. Liu, S. Wang, X. Zhang, and P. K. Shen, "Ultrathin Co_3O_4-Pt core-shell nanoparticles coupled with three-dimensional graphene for oxygen reduction reaction," *International Journal of Hydrogen Energy*, vol. 46, no. 17, pp. 10303–10311, 2021.

[12] H. Nan, X. Tian, L. Yang, T. Shu, H. Song, and S. Liao, "A platinum monolayer core-shell catalyst with a ternary alloy nanoparticle core and enhanced stability for the oxygen reduction reaction," *Journal of Nanomaterials*, vol. 2015, Article ID 715474, 11 pages, 2015.

[13] J. X. Wang, Y. Zhang, C. B. Capuano, and K. E. Ayers, "Ultralow charge-transfer resistance with ultralow Pt loading for hydrogen evolution and oxidation using Ru@Pt core-shell nanocatalysts," *Scientific Reports*, vol. 5, no. 1, Article ID 12220, 2015.

[14] K. Elbert, J. Hu, Z. Ma et al., "Elucidating hydrogen oxidation/evolution kinetics in base and acid by enhanced activities at the optimized Pt shell thickness on the Ru core," *ACS Catalysis*, vol. 5, no. 11, pp. 6764–6772, 2015.

[15] Y.-F. Xing, Y. Zhou, Y.-B. Sun et al., "Bifunctional mechanism of hydrogen oxidation reaction on atomic level tailored-Ru@Pt core-shell nanoparticles with tunable Pt layers," *Journal of Electroanalytical Chemistry*, vol. 872, Article ID 114348, 2020.

[16] J. Hu, K. A. Kuttiyiel, K. Sasaki, C. Zhang, and R. R. Adzic, "Determination of hydrogen oxidation reaction mechanism based on Pt–H_{ad} energetics in alkaline electrolyte," *Journal of the Electrochemical Society*, vol. 165, no. 15, pp. J3355–J3362, 2018.

[17] J. Cai, X. Liao, P. Li et al., "Penta-twinned Rh@Pt core-shell nanobranches with engineered shell thickness for reversible and active hydrogen redox electrocatalysis," *Chemical Engineering Journal*, vol. 429, Article ID 132414, 2022.

[18] X.-M. Lin, X.-T. Wang, Y.-L. Deng et al., "*In situ* probe of the hydrogen oxidation reaction intermediates on Pt Ru a bimetallic catalyst surface by core-shell nanoparticle-enhanced raman spectroscopy," *Nano Letters*, vol. 22, no. 13, pp. 5544–5552, 2022.

[19] K. P. Kepp, "A quantitative scale of oxophilicity and thiophilicity," *Inorganic Chemistry*, vol. 55, no. 18, pp. 9461–9470, 2016.

[20] E. Antolini and E. R. Gonzalez, "The electro-oxidation of carbon monoxide, hydrogen/carbon monoxide and methanol in acid medium on Pt-Sn catalysts for low-temperature fuel cells: a comparative review of the effect of Pt-Sn structural characteristics," *Electrochimica Acta*, vol. 56, pp. 1–14, 2010.

[21] 2022 , https://www.bloomberg.com/markets/commodities/futures/metals.

[22] D. González-Quijano, W. J. Pech-Rodríguez, J. I. Escalante-García, G. Vargas-Gutiérrez, and F. J. Rodríguez-Varela, "Electrocatalysts for ethanol and ethylene glycol oxidation reactions. Part I: Effects of the polyol synthesis conditions on the characteristics and catalytic activity of Pt–Sn/C anodes," *International Journal of Hydrogen Energy*, vol. 39, pp. 16676–16685, 2014.

[23] D. González-Quijano, W. J. Pech-Rodríguez, J. A. González-Quijano et al., "Performance and in-situ FTIR evaluation of Pt-Sn/C electrocatalysts with several Pt : Sn atomic ratios for the ethanol oxidation reaction in acidic media," *Chemelectrochem*, vol. 5, no. 22, pp. 3540–3547, 2018.

[24] X. Wang, L. Altmann, J. Stöver et al., "Pt/Sn intermetallic, core/shell and alloy nanoparticles: colloidal synthesis and structural control," *Chemistry of Materials*, vol. 25, no. 8, pp. 1400–1407, 2013.

[25] M. M. S. Pupo, F. E. López-Suárez, A. Bueno-López, C. T. Meneses, K. I. B. Eguiluz, and G. R. Salazar-Banda, "Sn@Pt and Rh@Pt core–shell nanoparticles synthesis for glycerol oxidation," *Journal of Applied Electrochemistry*, vol. 45, pp. 139–150, 2015.

[26] Y. Holade, C. Morais, S. Arrii-Clacens, K. Servat, T. W. Napporn, and K. B. Kokoh, "New preparation of PdNi/C and PdAg/C nanocatalysts for glycerol electrooxidation in alkaline medium," *Electrocatalysis*, vol. 4, no. 3, pp. 167–178, 2013.

[27] Y. Holade, K. Servat, T. W. Napporn, and K. B. Kokoh, "Electrocatalytic properties of nanomaterials synthesized from "bromide anion exchange" method—investigations of glucose and glycerol oxidation," *Electrochimica Acta*, vol. 162, pp. 205–214, 2015.

[28] Y. Holade, R. G. da Silva, K. Servat et al., "Facile synthesis of highly active and durable PdM/C (M = Fe, Mn) nanocatalysts for the oxygen reduction reaction in an alkaline medium," *Journal of Materials Chemistry*, vol. 4, no. 21, pp. 8337–8349, 2016.

[29] Y. Holade, N. E. Sahin, K. Servat, T. W. Napporn, and K. B. Kokoh, "Recent advances in carbon supported metal nanoparticles preparation for oxygen reduction reaction in low temperature fuel cells," *Catalysts*, vol. 5, no. 1, pp. 310–348, 2015.

[30] S. Dessources, C. Morais, T. W. Napporn, and K. B. Kokoh, "Reversible electrocatalytic activity of carbon-supported Pt_xNi_{1-x}in hydrogen reactions," *ChemPhysChem*, vol. 17, no. 23, pp. 3964–3973, 2016.

[31] J. C. Carrillo-Rodríguez, A. M. Garay-Tapia, B. Escobar-Morales et al., "Insight into the performance and stability of N-doped Ordered Mesoporous Carbon Hollow Spheres for the ORR: Influence of the nitrogen species on their catalytic activity after ADT," *International Journal of Hydrogen Energy*, vol. 46, pp. 26087–26100, 2021.

[32] O. J. Duarte-Urbina, F. J. Rodríguez-Varela, F. Fernández-Luqueño et al., "Bioanodes containing catalysts from onion waste and *Bacillus subtilis* for energy generation from pharmaceutical wastewater in a microbial fuel cell," *New Journal of Chemistry*, vol. 45, no. 28, pp. 12634–12646, 2021.

[33] A. Hernández-Ramírez, F. J. Rodríguez-Varela, P. C. Meléndez-González, and M. E. Sánchez-Castro, "Catalytic activity of Pt–CoTiO3 nanocatalysts supported on reduced graphene oxide functionalized with Cr organometallic compounds for the oxygen reduction reaction," *Journal of Materials Research*, vol. 36, pp. 4192–4206, 2021.

[34] A. A. Siller-Ceniceros, M. E. Sánchez-Castro, D. Morales-Acosta, J. R. Torres-Lubian, E. Martínez, and F. J. Rodríguez-Varela, "Innovative functionalization of Vulcan XC-72 with Ru organometallic complex: Significant enhancement in catalytic activity of Pt/C electrocatalyst for the methanol oxidation reaction (MOR)," *Applied Catalysis B: Environmental*, vol. 209, pp. 455–467, 2017.

[35] J. Shi, J. Wang, Y. Chen, Y. Sun, B. Liu, and Y. Fan, "Ag-Pd core-shell electrocatalysts for ethanol oxidation and oxygen reduction reactions in alkaline medium," *Journal of Physics: Materials*, vol. 4, no. 1, Article ID 014002, 2021.

[36] Y. Yang, C. Tan, Y. Yang et al., "Pt_3 Co@Pt Core@shell nanoparticles as efficient oxygen reduction electrocatalysts in direct methanol fuel cell," *ChemCatChem*, vol. 13, no. 6, pp. 1587–1594, 2021.

[37] F. Mansoori Mosleh, Y. Mortazavi, N. Hosseinpour, and A. A. Khodadadi, "Asphaltene adsorption onto carbonaceous nanostructures," *Energy and Fuels*, vol. 34, no. 1, pp. 211–224, 2020.

[38] T. C. S. Evangelista, G. T. Paganoto, M. C. C. Guimarães, and J. Ribeiro, "Raman spectroscopy and electrochemical investigations of Pt electrocatalyst supported on carbon prepared through plasma pyrolysis of natural gas," *Journal of Spectroscopy*, vol. 2015, Article ID 329730, 2015.

[39] L. Wang, Y. Wang, M. Wu et al., "Nitrogen, fluorine, and boron ternary doped carbon fibers as cathode electrocatalysts for zinc-air batteries," *Small*, vol. 14, no. 20, Article ID 1800737, 2018.

[40] R. Wang, H. Wang, H. Li et al., "An Fe@Fe3C-inserted carbon nanotube/graphite composite support providing highly dispersed Pt nanoparticles for ethanol oxidation," *Electrochimica Acta*, vol. 132, pp. 251–257, 2014.

[41] A. U. Haq, S. Askari, A. McLister et al., "Size-dependent stability of ultra-small α-/β-phase tin nanocrystals synthesized by microplasma," *Nature Communications*, vol. 10, no. 1, p. 817, 2019.

[42] F. Trombetta, D. W. Lima, F. Fiegenbaum, M. R. Becker, M. O. de Souza, and E. M. Martini, "C16MI.OTf ionic liquid on Pt/C and PtMo/C anodes improves the PEMFC performance," *International Journal of Hydrogen Energy*, vol. 43, no. 14, pp. 6945–6953, 2018.

[43] J. C. Martínez-Loyola, A. A. Siller-Ceniceros, M. E. Sánchez-Castro et al., "High performance Pt nanocatalysts for the oxidation of methanol and ethanol in acid media by effect of functionalizing carbon supports with Ru organometallic compounds," *Journal of the Electrochemical Society*, vol. 167, no. 16, Article ID 164502, 2020.

[44] C. A. Campos-Roldán, G. Ramos-Sánchez, R. G. Gonzalez-Huerta, J. R. Vargas García, P. B. Balbuena, and N. Alonso-Vante, "Influence of sp^3-sp^2 carbon nanodomains on metal/support interaction, catalyst durability, and catalytic activity for the oxygen reduction reaction," *ACS Applied Materials and Interfaces*, vol. 8, no. 35, pp. 23260–23269, 2016.

[45] J. Zou, M. Wu, S. Ning, L. Huang, X. Kang, and S. Chen, "Ru@Pt core–shell nanoparticles: impact of the atomic ordering of the Ru metal core on the electrocatalytic activity of the Pt shell," *ACS Sustainable Chemistry & Engineering*, vol. 7, no. 9, pp. 9007–9016, 2019.

[46] P. Ochal, J. L. Gomez de la Fuente, M. Tsypkin et al., "CO stripping as an electrochemical tool for characterization of Ru@Pt core-shell catalysts," *Journal of Electroanalytical Chemistry*, vol. 655, no. 2, pp. 140–146, 2011.

[47] C. M. Pedersen, M. Escudero-Escribano, A. Velázquez-Palenzuela, L. H. Christensen, I. Chorkendorff, and I. E. L. Stephens, *Electrochimica Acta*, vol. 179, pp. 647–657, 2015.

[48] J. Zheng, Y. Yan, and B. Xu, "Correcting the hydrogen diffusion limitation in rotating disk electrode measurements of hydrogen evolution reaction kinetics," *Journal of the Electrochemical Society*, vol. 162, no. 14, pp. F1470–F1481, 2015.

[49] S. Anantharaj, S. R. Ede, K. Karthick et al., "Precision and correctness in the evaluation of electrocatalytic water splitting: revisiting activity parameters with a critical assessment," *Energy & Environmental Science*, vol. 11, no. 4, pp. 744–771, 2018.

[50] C. Wei, R. R. Rao, J. Peng et al., "Recommended practices and benchmark activity for hydrogen and oxygen electrocatalysis in water splitting and fuel cells," *Advances in Materials*, vol. 31, Article ID 1806296, 2019.

[51] Á. Selva-Ochoa, J. Su-Gallegos, P. J. Sebastian, L. Magallón-Cacho, and E. Borja-Arco, "Hydrogen oxidation and oxygen reduction reactions on an OsRu-based electrocatalyst synthesized by microwave irradiation," *Materials*, vol. 14, no. 19, p. 5692, 2021.

[52] N. Ramaswamy, S. Ghoshal, M. K. Bates, Q. Jia, J. Li, and S. Mukerjee, "Hydrogen oxidation reaction in alkaline media: relationship between electrocatalysis and electrochemical double-layer structure," *Nano Energy*, vol. 41, pp. 765–771, 2017.

[53] W. Sheng, H. A. Gasteiger, and Y. Shao-Horn, "Hydrogen oxidation and evolution reaction kinetics on platinum: acid vs alkaline electrolytes," *Journal of the Electrochemical Society*, vol. 157, no. 11, pp. B1529–B1536, 2010.

[54] W. Sheng, Z. Zhuang, M. Gao, J. Zheng, J. G. Chen, and Y. Yan, "Correlating hydrogen oxidation and evolution activity on platinum at different pH with measured hydrogen binding energy," *Nature Communications*, vol. 6, no. 1, p. 5848, 2015.

[55] S. Panigrahy, R. Samanta, P. Panda, R. Mishra, and S. Barman, "RuO_2 as promoter in Pt-RuO_2-nanostructures/carbon composite, a pH universal catalyst for hydrogen evolution/oxidation reactions," *International Journal of Energy Research*, vol. 46, no. 5, pp. 6406–6420, 2022.

[56] P. Wang, H. Cui, and C. Wang, "Ultrathin PtMo-CeO hybrid nanowire assemblies as high-performance multifunctional catalysts for methanol oxidation, oxygen reduction and hydrogen oxidation," *Chemical Engineering Journal*, vol. 429, Article ID 132435, 2022.

[57] R. Samanta, R. Mishra, and S. Barman, "Interface-engineered porous Pt–PdO nanostructures for highly efficient hydrogen evolution and oxidation reactions in base and acid," *ACS Sustainable Chemistry & Engineering*, vol. 10, no. 11, pp. 3704–3715, 2022.